Heliyon 9 (2023) e19808

Contents lists available at ScienceDirect

Heliyon

journal homepage: www.cell.com/heliyon

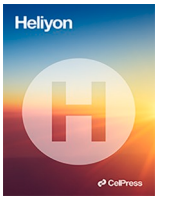

AB-INITIO study of electronic, mechanical, optical and thermoelectric properties of $KGeCl_3$ for photovoltaic application

Mohammed ElSaid Sarhani [a,*], Tahar Dahame [a], Mohamed Lamine Belkhir [a], Bachir Bentria [a], Anfal Begagra [b]

[a] Materials Physics Laboratory, Amar Thlidji University, Laghouat, Algeria
[b] Materials Laboratory for Applications and Valorization of Renewable Energy, Amar Thlidji University, Laghouat, Algeria

ARTICLE INFO

Keywords:
$KGeCl_3$
PSCs
Lead-free based perovskite
First principle
Thermoelectric

ABSTRACT

In this theoretical study, the potential of $KGeCl_3$ was investigated as a lead-free perovskite active layer for perovskite solar cells. Calculations of the structural, electronic, elastic, optic, and thermoelectric properties of $KGeCl_3$ in its cubic, tetragonal, and orthorhombic phases were performed using the generalized gradient approximation (GGA) within the wien2k package. The findings demonstrated that the tetragonal crystalline structure of KGeCl3 exhibited the least energy content, rendering it the most thermodynamically stable phase. It was found that the electronic band structure of $KGeCl_3$ exhibited a direct band gap of 0.92 eV, thus positioning it as a material with promise for utilization as a photovoltaic absorber. Furthermore, the elastic properties of $KGeCl_3$ were calculated, indicating the presence of suitable mechanical stability for practical applications. Additionally, the optical properties and thermoelectric performance of $KGeCl_3$ were examined, thereby highlighting its potential for incorporation into thermoelectric devices. In summary, our research showcases how $KGeCl_3$ holds significant promise as a viable substitute for lead-based perovskite materials in applications such as solar cells and other optoelectronic devices.

1. Introduction

Perovskite materials present captivating possibilities for solar cell usage, mainly due to their impressive optical and electrical capabilities. These include a direct band gap, broad-spectrum light absorption, excellent carrier mobility, low excitation binding energy around 2 meV, and extended diffusion length [1]. Furthermore, the potential manageability of perovskite film excellence renders it advantageous in contrast to alternative materials. This assertion is supported by various techniques capable of diminishing defect density, thereby resulting in improved performance [2].

Lead-containing perovskite materials find widespread utilization in perovskite solar cells (PSCs), employing compounds like methylammonium (MA) and formamidinium (FA) lead halides [3]. Notably, the pinnacle of power conversion efficiency, reaching around 25%, has been realized in lead halide solar cells utilizing MA-PbI_3 as the active layer [4].

The initial documentation of halide perovskites with an organic-inorganic composition dates back to 1884 and 1892. Subsequently, in 1978 and 1995, studies emerged concerning lead halides involving MA and FA, which have since become widely utilized

* Corresponding author.
E-mail address: m.sarhani@lagh-univ.dz (M.E. Sarhani).

https://doi.org/10.1016/j.heliyon.2023.e19808
Received 6 June 2023; Received in revised form 1 September 2023; Accepted 1 September 2023
Available online 2 September 2023

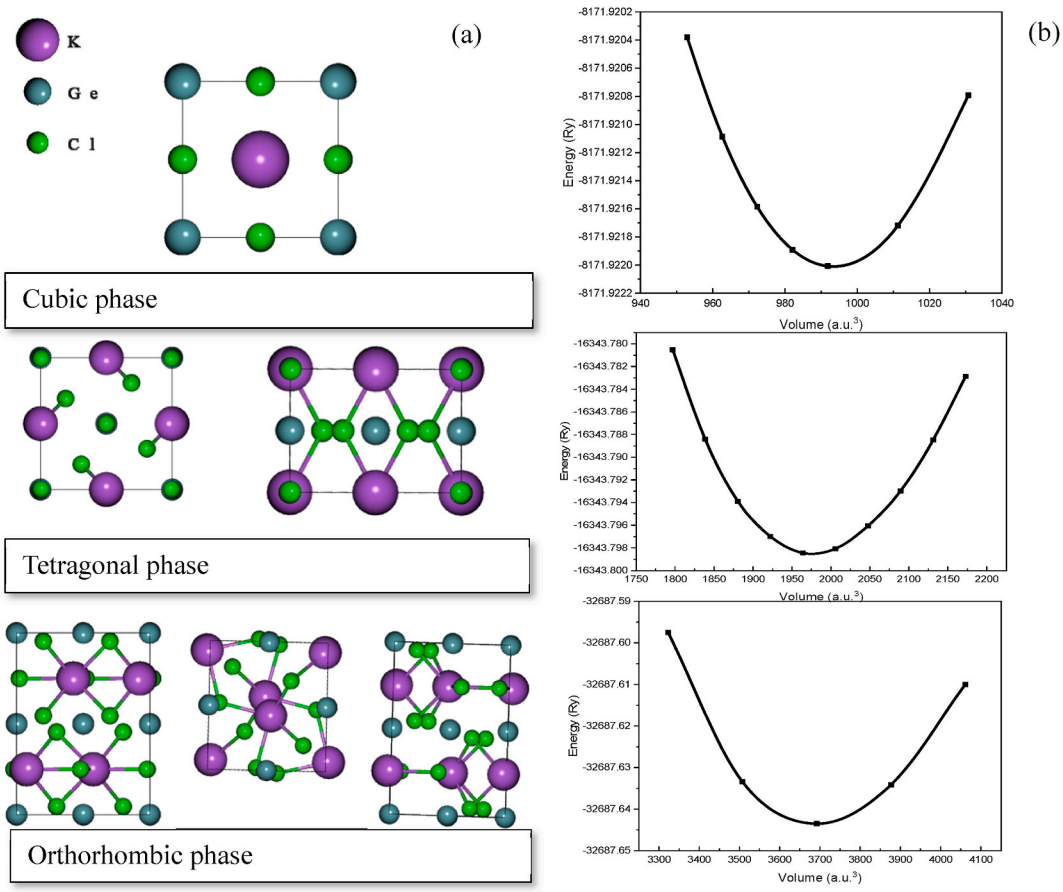

Fig. 1. Overview for different phases of $KGeCl_3$ (a), and the variation of total energy of each phase of $KGeCl_3$ as function of the unit cell volume (b).

components in perovskite solar cells [5]. After many years later, in a conference presentation in Japan 2006 the perovskite materials were reported as an absorber for solar cells [6–9]. Subsequently, these materials have garnered substantial interest in recent years owing to their notable efficacy, facile manufacturability, and economic viability [10]. In 2014, Feng Liu et al. [11], reported a high PCE of over 14% for a solar cell device containing $CH_3NH_3PbI_3$ as an absorber. They used the AMPS simulator program for adding more understanding of the role of each compound in solar cells and their effects. In 2017 an efficiency of over 31% was reported by Usha Mandadapu et al. [12], they used SCAPS-1D to simulate a device with $CH3NH3PbI_3$ as the light-absorbing layer, and (6,6)-phenyl--C61-butyric acid methyl ester (PCBM) and poly(3,4-ethylenedioxythiophene) polystyrene sulfonate (PEDOT: PSS) as the electron transport material (ETM) and hole transport material (HTM), respectively. While the experiment reached 5% of power conversion efficiency as it is reported by Arun Singh Chouhan et al., in 2018 [13].

However, the presence of harmful heavy metals like lead throughout the lifecycle of perovskite solar cells (PSCs) raises significant environmental concerns [14]. Encouragingly, alternative, less toxic elements including Titanium (Ti), Germanium (Ge), Tin (Sn), Antimony (Sb), and Bismuth (Bi) have been shown to replace lead in PSCs. Recent advancements, like FA-SnI_3 and SnI_3, have paved the way for environmentally safer PSCs [15]. Consequently, the pursuit of stable and efficient perovskite materials has become a lively area of research in photovoltaics. Several theoretical studies have explored the energy band gap potential of halide perovskites using density functional theory calculations [16–20]. Recent inquiries have been directed towards the $KGeCl_3$ perovskite, encompassing examinations of its electronic and optical characteristics. Employing ab-initio calculations, M. Houari et al. conducted a study in 2020 [17] to scrutinize the structural, elastic, and optoelectronic attributes of the cubic-phase $KGeCl_3$ perovskite utilizing GGA-PBE (mbj-GGA) approximations. They found that it is a semiconductor with a direct bandgap of 0.9(1.27) eV and a high absorption coefficient in the light energy range. Similarly, I. Hamideddine et al. [21] investigated the electronic and optical properties of the cubic phase of $KGeCl_3$ perovskite. They take into account the spin-orbit interaction in the calculation, and they find its bandgap energy equal to 0.95 eV the same as it is without spin orbit coupling (SOC), due to the absence of any heavy elements in $KGeCl_3$. In addition to the cubic phase, M. Mauwa Namisi et al. [22] examined how $KGeCl_3$ compound in its tetragonal and trigonal phases behave in terms of their electronic and optical characteristics. They find the same bandgap of $KGeCl_3$ in cubic, but it expands to 1.2 eV and 2.7 eV in tetragonal and trigonal phases, respectively.

In this study, we have employed the Wien2k package, a proficient ab initio software recognized for its commendable reproducibility in computing diverse physical parameters [23], was harnessed. The aim was to scrutinize the electronic, elastic, optical, and

Table 1
The lattice parameters a_i in Å of relaxed structure compared with those from prior studies, bulk modulus B_0 in GPa and its derivatives, and formation energy in eV for the $KGeCl_3$ calculated wilth GGA-PBE.

	a_i (A)	B_0 (GPa)	B'	E_f (eV)
Cubic	5.28[5.27[a] 5.57[b] 5.29[c]]	27.110	4.325	−0.095
Tetragonal	7.38, 5.31	27.529	4.448	−0.165
Orthorhombic	7.60, 10.33, 6.97	31.054	4.575	−0.098

[a] = [22] GGA:PP:GGA (GW).
[b] = [35] GGA:Lapw + mbj
[c] = [21] GGA:Lapw + SOC.

thermoelectric attributes of the $KGeCl_3$ perovskite across its cubic, tetragonal, and orthorhombic phases. Ab initio calculations are powerful tools for investigating the physicochemical properties of solids, diverse organic and inorganic molecules. Their strengths lie in their ability to provide accurate electronic structure information, enabling the prediction of molecular geometries, electronic properties [24], and vibrational spectra. DFT is particularly well-suited for large systems, making it valuable for studying complex molecules. They also considered to be "reproducible" because they are based on fundamental principles of quantum mechanics and do not rely on empirical fitting parameters [25,26]. However, DFT simulations have limitations too. They may struggle with accurately describing van der Waals interactions, dispersion forces, and strong correlation effects, leading to potential inaccuracies in certain systems. Additionally, the choice of exchange-correlation functional can greatly influence results, making it essential to select an appropriate functional for specific investigations [27]. The anisotropic properties of the perovskite were characterized by calculating the directional dependence of various properties such as the bulk and young modulus. The optical characteristics of $KGeCl_3$ were assessed employing the density functional perturbation theory (DFPT) methodology, while the thermoelectric attributes were explored through the application of the Boltzmann transport theory.

2. Calculation methods and computational details

All computations conducted in this study rely on Ab-initio calculations full potential linear augmented plane-wave (FP-LAPW) method, as realized through the Wien2k package [28]. The Perdew-Burke-Eenzerhof (PBE) was employed to characterize the interaction involving exchange and correlation among the valence electrons [29], but spin-orbit coupling was neglected. The foundational functions within the interstitial spaces were expanded to a limit of $R_{mt}*K_{max} = 7.0$, with R_{mt} representing the minimum muffin-tin sphere radius and Kmax signifying the highest reciprocal lattice vector employed in the plane wave expansion. The (R_{mt}) used were 2.5, 2.49, 2.49 a. u. for K, Ge, and Cl, respectively. The cutoff energy, demarcating the distinction between valence and core states, was elected as 102 eV. The self-consistency of calculations (SCF) was selected as 10–5 e/bohr3 and $18 \times 18 \times 18$, $13 \times 13 \times 18$, and $13 \times 13 \times 18$ Monkhorst-Pack [30] grid for cubic, tetragonal, and orthorhombic phases, respectively.

The electronic and optical attributes were calculated employing the identical parameters obtained from structural optimization. The elastic constants were computed utilizing Charpin [31] and the "finite-strain" [32] methods which were incorporated in wien2k and CASTEP codes.

3. Results and discussion

3.1. Structural properties

The alkali halide perovskite $KGeCl_3$ crystallizes in cubic, tetragonal, and orthorhombic with (Pm-3m 221), (P4/mbm 127) and (Pnam 62) space groups [22,33]. Fig. 1(a) shows the side view of cubic structure, top and (xz) side view of tetragonal structure, and top, (xz) and (yz) sides of orthorhombic structure, of $KGeCl_3$ perovskite. Structural optimizations were performed first to determine the equilibrium lattice constants. The cubic and tetragonal crystals are optimized by minimizing the external and internal forces and charges starting from parameters found by M. Mauwa Namisi et al. [22]. The variation of total energy with primitive cell's volume for all phases is presented in Fig. 1(b). The highest energy release at the smallest volume (V_0) was employed within the Birch-Murnaghan equation of state [34] to compute the fundamental state values of lattice constants (a_i; i = 1,2,3) and bulk modulus (B_0) and its derivative (B'), for cubic, tetragonal and orthorhombic phases of $KGeCl_3$. Thermodynamic stabilities are assessed through the computation of formation energies (Ef) for each phase, utilizing the subsequent relationship {1}:

$$E_f = E(KGeCl_3) - E(KCl) - E(GeCl_2) \quad (1)$$

Therefore, this fact guarantees the chemical stability of the compound and provides a ground for synthesizing them. The obtained a_i, B_0, B', and E_f values are presented in Table 1 and where they are found to corroborate the previously published results for cubic and tetragonal phases.

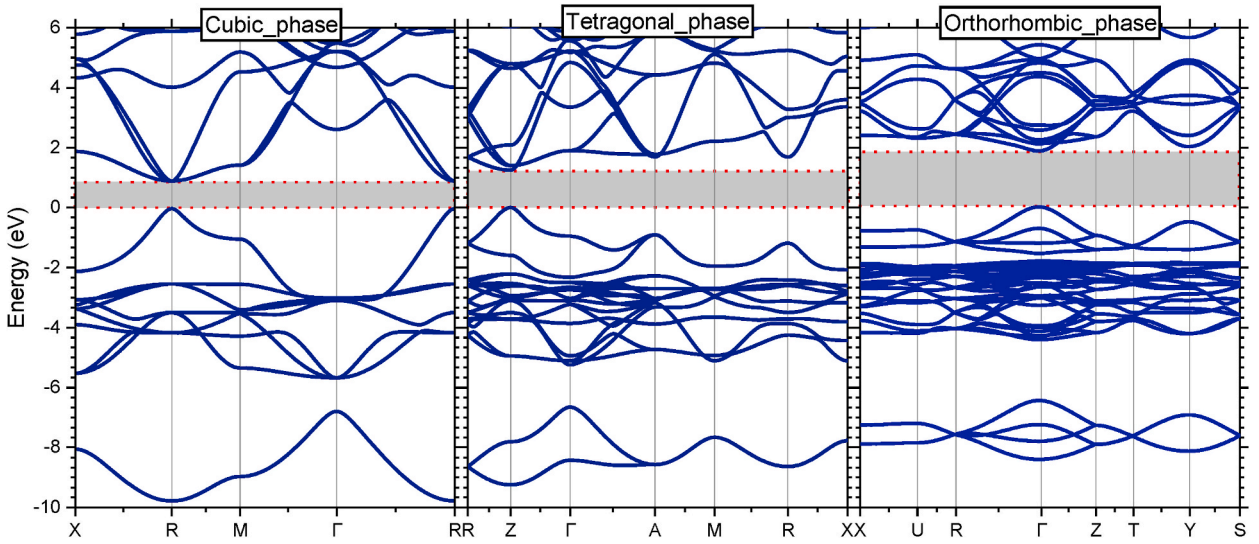

Fig. 2. Electronic energy band structures were computed along the K-path within the first Brillouin zone for $KGeCl_3$ compound, employing the GGA-PBE method.

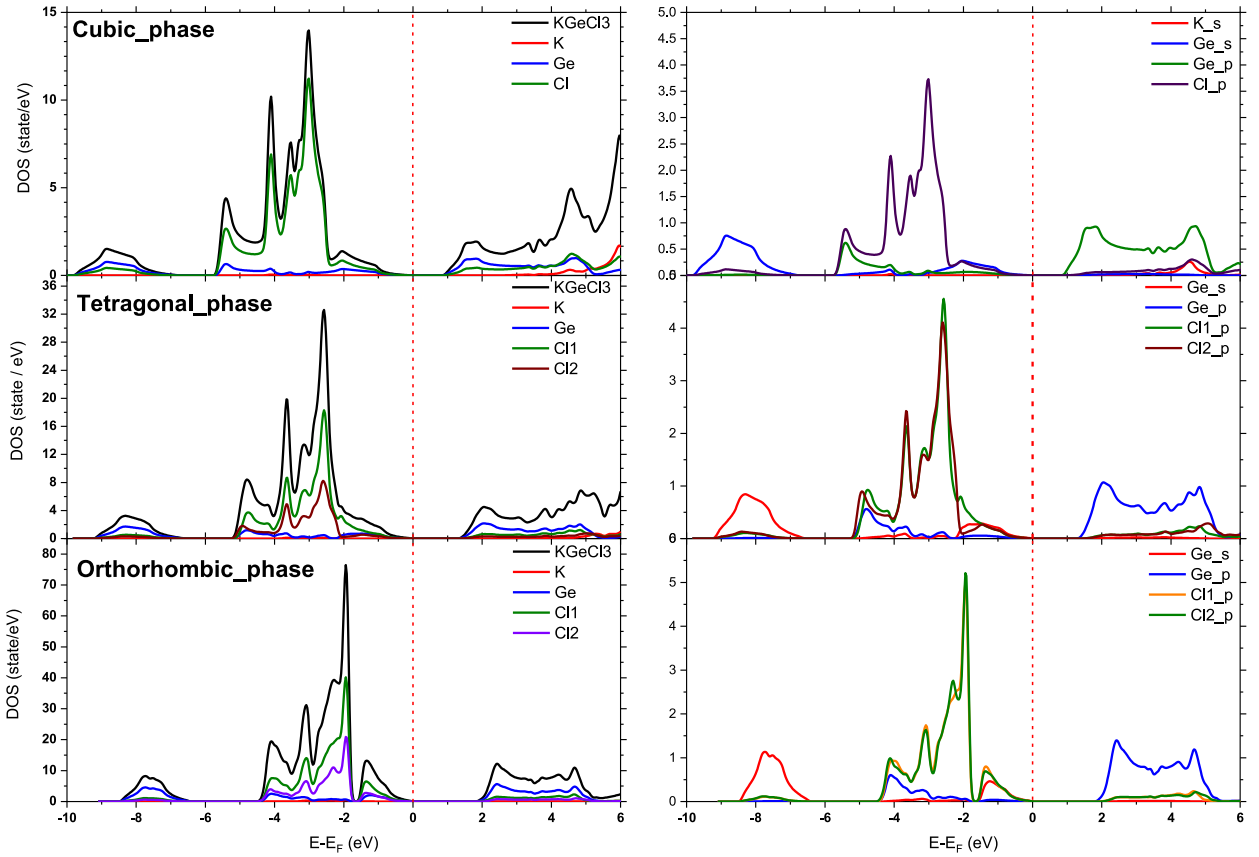

Fig. 3. Calculated T-DOS (right side) and P-DOS (left side) of $KGeCl_3$ perovskite in cubic, tetragonal and orthorhombic phases.

Table 2
Effective Masses of Electron m_e, Hole m_h, of cubic, tetragonal and orthorhombic structures of $KGeCl_3$, calculated using transM code.

	Cubic		Tetragonal		orthorhombic	
	$m_e(m_0)$	$m_h(m_0)$	$m_e(m_0)$	$m_h(m_0)$	$m_e(m_0)$	$m_h(m_0)$
$KGeCl_3$	0.32 10.78[a]	0.11 10.71[a]	0.26	0.17	0.49	0.44
$RbGeCl_3$	0.24[b]	0.24[b]				
$CsGeCl_3$	0.27[b]	0.28[b]				

[a] = [21].
[b] = [43].

Table 3
Calculated elastic constants of studied phases of $KGeCl_3$ compound.

C_{ij}(GPa)	C_{11}	C_{12}	C_{13}	C_{22}	C_{23}	C_{33}	C_{44}	C_{55}	C_{66}
Cubic	53.29 56.16[a] 56.74[b]	10.21 09.12[a] 11.19[b]					8.42 8.34[a] 7.77[b]		
Tetragonal	34.61 43.85[a]	19.40 25.02[a]	14.16 14.0[a]			58.37 60.64[a]	10.21 10.59[a]		18.84 22.30[a]
Orthorhombic	49.37	18.15	25.42	41.71	18.26	37.57	7.56	15.81	11.65

[a] = [22].
[b] = [35].

3.2. Electronic properties

3.2.1. Band structure

Several pieces of information about physical properties, like optical nature, thermoelectric behavior, and charge transport [36–39] can be obtained from the band structure (BS). For each phase of $KGeCl_3$, BS calculation was performed along the symmetry direction in the Brillouin zone. Our findings are displayed in Fig. 2. Observations reveal that the maximum of valence band (VB_M) and the minimum of conduction band (CB_M) are situated at the same high-symmetry points across all phases. This means that $KGeCl_3$ in all phases is a semiconductor with a direct band gap. For cubic structure, a band gap of 0.92 eV is located at the R point. This result is very close to previously calculated results (0.8 eV using PP: GGA under quantum espresso [22], 0.9 eV using FP: GGA under wien2k [30], 0.95 eV using FP: GGA with SOC under wien2k [21]). while it is located at the Z point with a value of 1.26 eV for the tetragonal phase, which agrees with the calculated results in Ref. [22] which is 1.2 (FP: GGA used). The band gap energy of the orthorhombic phase is 1.88 eV located at Γ point.

3.2.2. Density of states

The total density of states (TDOS) and the partial density of states (PDOS) were calculated using GGA approximation and presented in Fig. 3. The Fermi level is set to be at 0 energy. Based on PDOS, we can find the orbitals that create the valence band and the conduction band, also the orbitals that dominate in each band. In Fig. 3, a visual representation is provided depicting TDOS as well as PDOS for $KGeCl_3$ compound. We see that the dominant orbital in the valence band is the p orbital of the Cl element (p-Cl) and to a lesser extent the *s*-Ge, while the p-Ge orbital dominates the conduction band in all phases. So, by controlling the presence and density of germanium in $KGeCl_3$ we can control its band gap energy.

3.2.3. Effective masses

The effective masses of electrons and holes are important parameters that determine the material's electrical and optical properties. Using the transM code, a tool developed by Refs. [40–42], we conducted computations to determine the effective masses of both electrons and holes within the $KGeCl_3$ perovskite. The obtained results are assumed in Table 2.

The effective mass of an electron or a hole is a measure of how easily it moves through the crystal lattice of the material. A smaller effective mass implies that the electron or hole can move more easily through the material, leading to higher mobility and better electrical conductivity.

The obtained effective mass values suggest that electrons have higher mobility than holes in $KGeCl_3$ perovskite cubic phase, as the electron's effective mass is smaller compared to the hole's effective mass. This is consistent with the behavior of a typical n-type semiconductor, where electrons are the majority carriers and have higher mobility than holes. From Table 2, we can see that the effective masses of electrons and holes are 0.32 and 0.11, respectively. These values are acceptable in comparison to effective masses of $RbGeCl_3$ and $CsGeCl_3$ perovskites studied by Ref. [43]. Conversely, the values of effective masses reported by Ref. [21] are much larger, which is not suitable for charge transportation. Overall, the obtained effective mass values for $KGeCl_3$ perovskite are promising and suggest that the material could be a good candidate for electronic and optoelectronic applications, especially compared to other similar materials in the article.

3.3. Mechanical properties

Because we're focused on understanding how materials hold up under stress and how their structure stays intact, we have

Table 4
Computed elastic modulus Cauchy pressure, average acoustic velocity, and Debye temperatures of studies crystalline structures of $KGeCl_3$ compound.

Parameters	Cubic	Tetragonal	Orthorhombic
B(GPa)	24.57 24.80[a] 26.37[b]	24.45 28.28[a]	27.75
G(GPa)	12.40 12.83[a] 12.17[b]	12.34 14.01[a]	11.00
E(GPa)	31.84 32.83[a] 31.64[b]	31.69 36.08[a]	29.16
ν	0.28 0.28[a] 0.30[b]	0.28 0.29[a]	0.32
C^P	1.79	9.19	10.59
$\bar{v}$ (m/s)	2448.43	2442.60	2270.24
B/G	1.98 1.93[a] 2.17[b]	2.70 2.02[a]	2.81
Θ_D (K)	236.09	236.71	224.10

[a] = [22].
[b] = [35].

Table 5
The computed anisotropic factors (A^U, A^B, A^E, A^Z) for the studied crystalline structures of $KGeCl_3$ compound.

Anisotropy factor	Cubic	Tetragonal	Orthorhombic
A^u	1.14	0.75	0.45
A^B	0	0.014	0.01
A^E	0.088	0.06	0.038
A^Z	0.391	1.343	0.484

calculated the elastic constants C_{ij}. The obtained values are listed in Table 3. The calculated elastic constants are positive and verify the stability criteria (C_{11}–$C_{12}>0$, $C_{11} > 0$, $C_{44} > 0$, $C_{11}+2C_{12} > 0$, and $C_{12}<B < C_{11}$) [44] which indicates that the $KGeCl_3$ compound is mechanically stable in all presented phases. The estimation of polycrystalline elastic modulus involves various approaches, including Voigt's, Reuss', and Hill's approximations [45]. Here we used Hill's approximation to calculate all the parameters related to elastic constants. The Cauchy pressure C^P, Young's modulus E, the shear modulus G, the ratio B/G, Average acoustic velocity $\bar{v}$, Debye temperatures Θ_D and Poisson's ratio ν are also calculated and summarized in Table .4.

A material's flexibility is characterized by a diminished Young's modulus, resulting in pronounced shape alterations. The reduced values of both bulk and shear moduli for $KGeCl_3$ perovskites signify their flexibility and softness, rendering them highly advantageous for applications involving thin films [33]. The values of the Poisson ratio, which are 28, 28, and 32%, suggest the dominant forces in this compound are the central forces, which appear between 25 and 50% [46]. The character of atomic bounding in solid materials relates to ductility and brutality and it could be found by considering C^P [47]. The computed C^P values for all $KGeCl_3$ phases exhibit positivity, indicating the material's metallic attributes and ductile behavior. Furthermore, the derived B/G ratio serves as an indicator of ductility. It can be said that the compound is ductile since its B/G larger than 1.75, and this is what we see achieved for all $KGeCl_3$ phases.

The Zener anisotropy factor (A^Z) holds pivotal information concerning the structural stability of a material. This factor serves as a significant indicator that sheds light on the material's propensity to exhibit differing mechanical responses along distinct crystallographic directions. Analyzing the Zener anisotropy factor provides valuable insights into the material's ability to maintain its structural integrity under various mechanical and environmental conditions. A^Z can be recast in the form [48,49].

$$A^Z = \frac{2C_{44}}{C_{11} - C_{12}} \tag{2}$$

The anisotropy percentage in bulk modulus A^B and Young modulus A^E is defined as [50–53].

$$A^B = \frac{B_V - B_R}{B_V - B_R} \tag{3}$$

$$A^E = \frac{E_V - E_R}{E_V - E_R} \tag{4}$$

where B_V and E_V are the anisotropies in Bulk A^B and Young A^E are related to universal anisotropy. As It recedes from zero, the crystal gets higher anisotropy. The universal anisotropy index A^U, Zener anisotropy factor A^Z, the percentage of anisotropies in the Bulk A^B, and the percentage of anisotropy in Young modulus A^E, are calculated using equations {2–4}. The results are presented in Table 5.

In order to observe the variations in different directions, we've generated both three-dimensional (3D) and two-dimensional (2D) anisotropic contour plots. These plots illustrate how properties like Young modulus (Fig. 4(a–c)) and Bulk modulus (Fig. 4(*d*–f)) change in the cubic (Fig. 4(a, d)), tetragonal (Fig. 4(b, e)), and orthorhombic (Fig. 4(c, f)) phases of $KGeCl_3$. Upon observation of Fig. 4, it becomes evident that $KGeCl_3$ markedly deviates from a spherical configuration in the depicted (3D) contour plots. This reaffirms the fact that $KGeCl_3$ possesses an anisotropic nature, meaning its properties aren't the same in all directions.

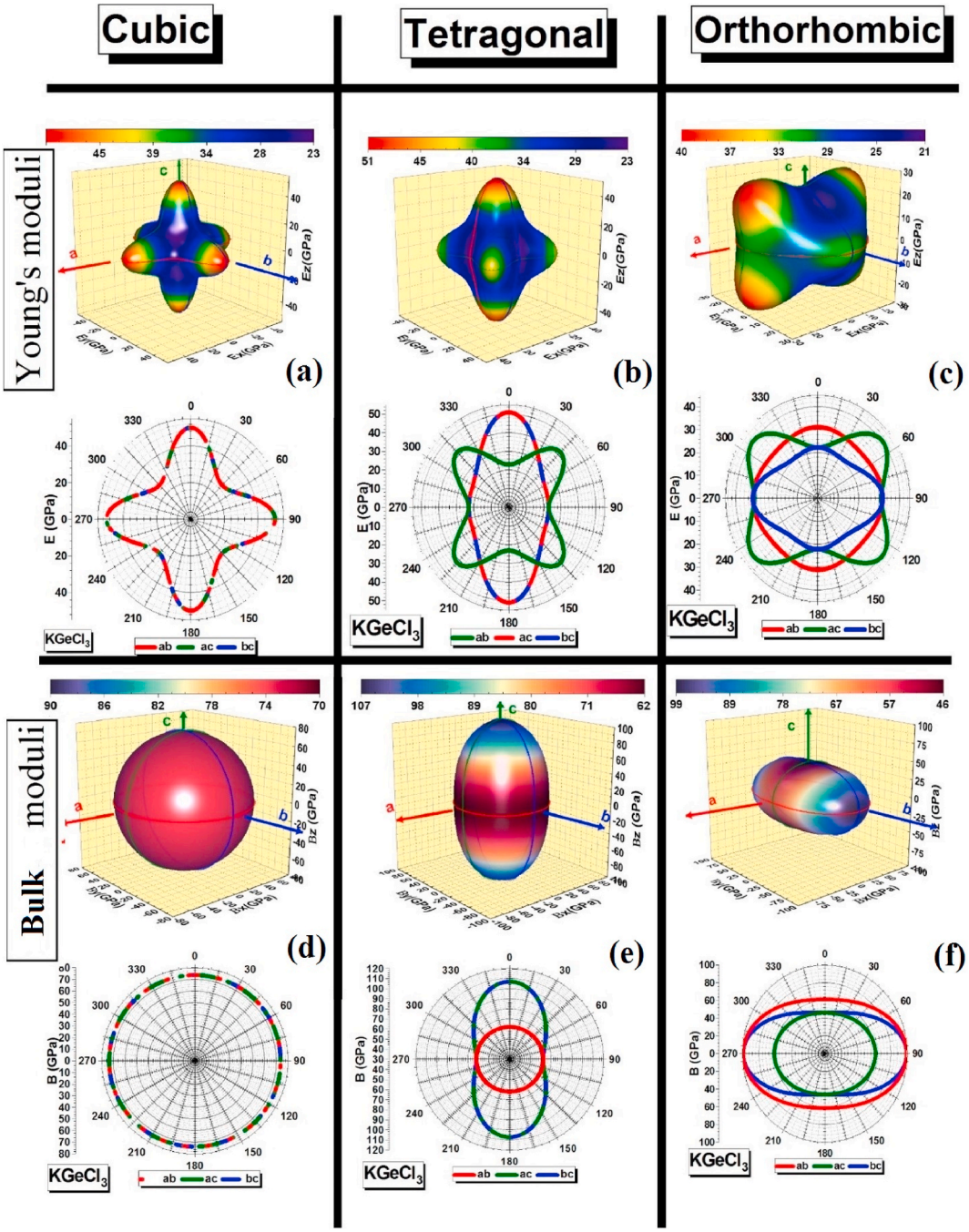

Fig. 4. The 3D and 2D anisotropic representation of Young's modulus and bulk modulus of $KGeC_3$ perovskite.

3.4. Optical properties

Solid materials have optical properties that can be employed in research and device applications [54–56]. The dielectric constant presents the substance permittivity ratio to the free space permittivity. The ability of a material to retain an electric field within its polarization, thereby characterizing its capacity, is referred to as permittivity. The complex dielectric function of a crystalline solid can be expressed by the equation {5} which presented below

$$\varepsilon(\omega) = \varepsilon_1(\omega) + i\varepsilon_2(\omega) \tag{5}$$

in this context, $\varepsilon_1(\omega)$ and $\varepsilon_2(\omega)$ denote the real and imaginary components of the dielectric function correspondingly. The real segment

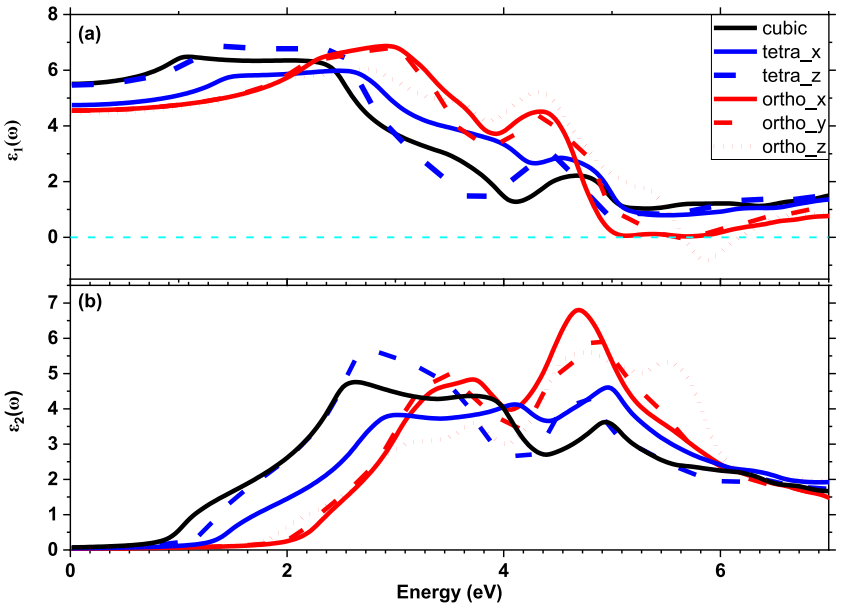

Fig. 5. Real ε_1 (ω) and Imaginary ε_2 (ω) part against the Photon Energy for each phase of $KGeCl_3$ perovskite.

Table 6
Static dielectric constants of $KGeCl_3$ perovskite.

	Cubic	Tetragonal	Orthorhombic
This work xx(yy)zz	5.47	4.75(5.47)	4.46
Other works	6.56 [22]	5.18 [22]	/

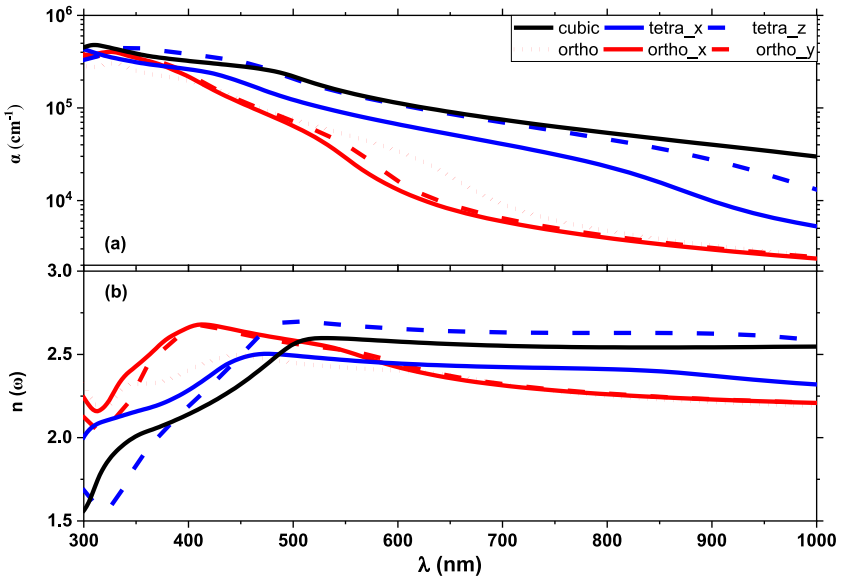

Fig. 6. The variation of the absorption coefficient (a) and refractive index (b) concerning wavelength in nm for the examined phases of the $KGeCl_3$ compound.

of the dielectric function directly governs the refractive characteristics, whereas the imaginary aspect governs the feasibility of inter-band electronic direct transitions corresponding to specific photon energy values [33]. In Fig. 5, the calculated dielectric function for $KGeCl_3$ in the studied phases is showcased, with (a) illustrating the real component ε_1 (ω) and (b) depicting the imaginary component ε_2 (ω) as functions of photon energy. The static dielectric constants for cubic, tetragonal, and orthorhombic phases of $KGeCl_3$ are

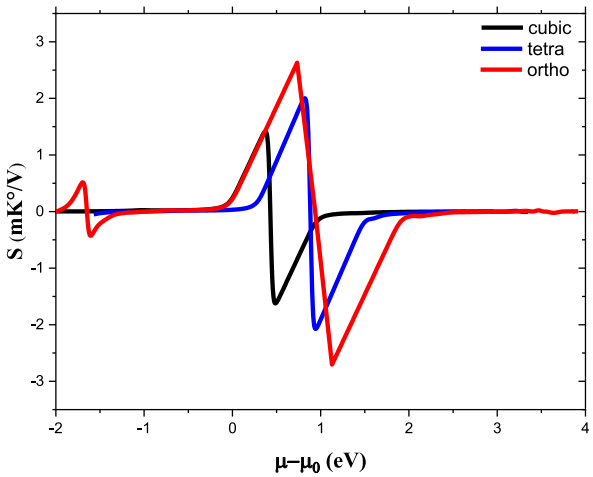

Fig. 7. The See-beck coefficients of $KGeCl_3$ against chemical potential.

assumed in Table 6.

The computed static dielectric constant for the cubic phase of $KGeCl_3$ is higher than its value in the tetragonal as well as orthorhombic crystalline structures of the same material. This result predicts that $KGeCl_3$ in the cubic phase is more sensitive to the optoelectric effect compared to other phases of $KGeCl_3$. The principal peaks within the $\varepsilon_2(\omega)$ spectrum correspond to transitions of electrons from the VB to the CB. Notably, the $\varepsilon_2(\omega)$ spectra exhibit a rapid ascent, culminating in the initial peak at 2.60 eV for cubic, 3.00 and 2.73 eV for the tetragonal phase in xx and ZZ orientations respectively, 3.50 and 3.17 eV for the orthorhombic phase in xx and zz orientations, respectively.

The optical properties such as the refractive index $n(\omega)$, and absorption coefficient $\alpha(\omega)$ are related to the dielectric function as equations {6, 7} which mentioned below

$$\alpha(\omega) = \sqrt{2}\omega\left[\sqrt{\varepsilon_1^2(\omega) + \varepsilon_2^2(\omega)} - \varepsilon_1(\omega)\right]^{1/2} \tag{6}$$

$$n(\omega) = \frac{1}{\sqrt{2}}\left[\sqrt{\varepsilon_1^2(\omega) + \varepsilon_2^2(\omega)} + \varepsilon_1(\omega)\right]^{1/2} \tag{7}$$

Fig. 6(a and b) presents the absorption coefficient in (cm^{-1}) and the refractive index per frequency (ω) as a function of wavelength in (nm). It is clear from Fig. 6(a) that $KGeCl_3$ has a high absorption ability. Its absorption coefficient is about 1×10^4 cm^{-1} for all photons in the visible range. In the solar spectrum, visible light is found within the range of wavelength $\lambda \approx 350$–800 nm which is translated to the energy of approximately 1.6–3.5 eV.

The $n(\omega)$ spectrum, is illustrated in Fig. 6(b). At zero photon energy, the static refractive index value is 2.34 for the cubic phase, 2.18, and 2.34 for the tetragonal phase in xx and zz orientations, while the orthorhombic phase has the lowest values of static refractive index which are 2.13 and 2.11 in xx and zz orientations. The emerged peaks from excitonic transitions can be seen. The peaks are more pronounced in the longer photon wavelength region than in the shorter photon wavelength region. The effect of excitonic tends to increase the oscillator strength [57].

3.5. Thermoelectric properties

Currently, energy is the main driver of industry and economy in the world. That is why researchers focus their attention towards the multiplicity of energy sources, and finding alternative sources that are renewable and environmentally friendly. Thermoelectric devices can provide a solution since they convert waste energy into electricity effectively improving the operational efficiency of engines, where a significant amount of energy is lost. We employed the Boltzmann Transport (Boltz Trap) code to calculate the electronic transport properties. Using the constant relaxation time approximation, we investigated different transport coefficients for the KGeCl3 perovskite at room temperature. These coefficients include Seebeck (S), electrical and thermal conductivities (σ/τ and K/τ), power factor (PF), as well as figure of merit (ZT), We've shown how these coefficients change across three distinct temperature ranges, all at 300 K°. Notably, there has been no previous exploration into the thermoelectric characteristics of the $KGeCl_3$ compound. The Seebeck effect, a material-specific property, quantifies the voltage ratio generated across a material exposed to a temperature gradient. This phenomenon entails the movement of charge carriers (electrons or holes) in response to temperature disparities, thereby prompting the creation of an electric current.

The variation in the Seebeck coefficient concerning the relative chemical potential μ with respect to the Fermi level μ_0. The μ_0 values are 0.127 Ry, 0.102 Ry, and 0.053 Ry for cubic, tetragonal in addition to orthorhombic phase of $KGeCl_3$, respectively, as

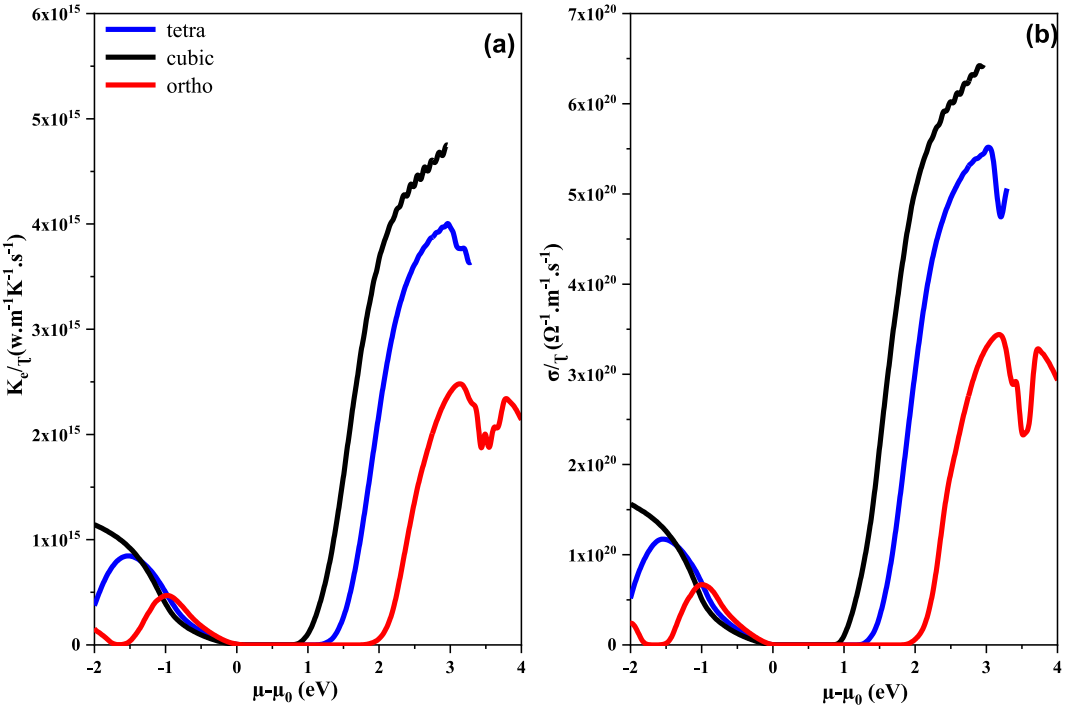

Fig. 8. (a) thermal and (b) electrical conductivities of $KGeCl_3$ in cubic, tetragonal and orthorhombic phases against chemical potential.

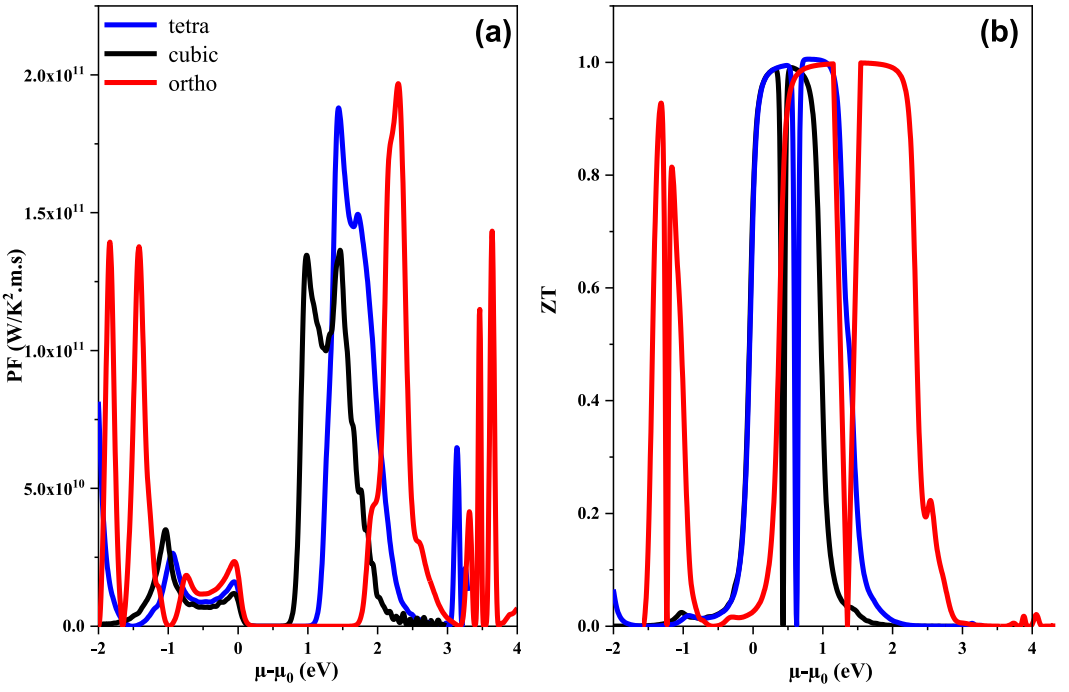

Fig. 9. (a) The power factor c) and figure of merit values of $KGeCl_3$ against chemical potential.

depicted in Fig. 7. From the Seebeck coefficient graphs, we can observe that the Seebeck coefficient (S) achieves 2.6, 2.0, and 1.4 mV/K for orthorhombic, tetragonal, and cubic respectively. These values are greater than that of germanium-based perovskite [58] and suggests that the material has strong thermoelectric performance.

How well a material can carry an electric current is determined by its electrical conductivity. This value is linked to how easily

charge carriers (like holes and electrons) can move around and how many of them are present in the material. The way free electrons contribute to how well $KGeCl_3$ can conduct electricity is explained by a factor called the electrical conductivity (σ/τ) coefficient. How this conductivity changes due to changes in the chemical potential is shown in Fig. 8(b). In Fig. 8(a), we can observe that as the energy levels increase from 0.9, 1.2, to 1.8 eV, the ability of $KGeCl_3$ to conduct heat, or its thermal conductivity, also increases. At energy levels of 2.96, 2.96, and 3.12 eV, the thermal conductivity peaks at 4.75×10^{15}, 3.97×10^{15}, and 2.48×10^{15} W/mK for the n-type region of the cubic, tetragonal, as well as orthorhombic phases of $KGeCl_3$.

We've presented the electronic thermal conductivity based on changes in chemical potential. By combining the electronic conductivity (k_e) and lattice conductivity (k_L), we determine the overall thermal conductivity ($k = k_e + k_L$). When two parts of a material experience different temperatures, the movement of electrons becomes more significant compared to the vibrations of atoms in the lattice. This results in the flow of electrons rather than phonon vibrations. This characteristic is crucial for developing effective materials used in converting heat into electrical currents [59,60]. As depicted in Fig. 8(a), the domain encompassing the chemical potential concerning the Fermi level showcased the most diminished thermal conductivity values. We see that the thermal conductivity curves are comparable to the electrical conductivity curves in terms of behavior for all phases of $KGeCl_3$. This demonstrates that where electric conductivity is present, the flow of electrons contributed to the transport of heat.

Fig. 9(b) illustrates the ability of $KGeCl_3$ perovskite to transform heat into practical electric energy, quantified by the figure of merit ZT, as it relates to changes in chemical potential. When using thermoelectric devices, materials with a greater ZT have higher efficiency. According to Fig. 9(b), ZT takes greater values in the ranges of 0.0 and 0.34 eV and 0.50–0.77 eV for cubic, 0.0 and 0.53 eV, and 0.70–1.17 eV for tetragonal, 0.0 and 0.73 eV and 1.15–1.77 eV for orthorhombic, but it falls to zero between these two ranges. The power factor $PF = S^2 \bullet \sigma$ is calculated, and the results are plotted as a function of chemical potential in Fig. 9(a). From these curves, it becomes apparent that the peak power factor occurs at approximately $\mu\text{-}\mu_0 = 0.9$ eV for the cubic phase, $\mu\text{-}\mu_0 = 1.4$ eV for the tetragonal phase, and $\mu\text{-}\mu_0 = 2.3$ eV for the orthorhombic phase of $KGeCl_3$.

4. Conclusion

The study of $KGeCl_3$ perovskite in different crystal structures and with different properties using LAPW-GGA approximation has provided valuable insights into the potential applications of this material. Our results show that $KGeCl_3$ perovskite has stable structures in all three crystal systems (cubic, tetragonal, and orthorhombic) and has good elastic properties, which makes it a promising material as a thin layer for use in photovoltaic technology and solar cells applications. According to the electronic band structure calculation, $KGeCl_3$ perovskite is a direct bandgap semiconductor with bandgap energies of 0.92 eV, 1.26 eV, and 1.88 eV for cubic, tetragonal, and orthorhombic phases, respectively. This implies that the material could be used in optoelectronic applications including photovoltaic devices. This study also revealed that $KGeCl_3$ perovskite has a relatively high absorption coefficient, which makes it a promising material for use in solar cells as an active layer. Finally, our computations pertaining to the thermoelectric attributes of $KGeCl_3$ perovskite propose its notably elevated thermoelectric efficiency, with a ZT value reaching 1 across all studied phases. This finding signifies its potential applicability within thermoelectric energy conversion devices. Overall, our study demonstrates the potential of $KGeCl_3$ perovskite as a multifunctional material with promising structural, electronic, optic, and thermoelectric properties across different crystal structures. These findings could inspire further investigations into the material's properties and potential applications in a wide range of fields.

Author contribution statement

Mohammed ElSaid SARHANI: Conceived and design the analysis; Analyzed and interpreted the data; Contributed analysis tools or data; Wrote the paper. Tahar DAHAME, Mohamed Lamine BELKHIR, Bachir BENTRIA, Anfal BEGAGRA: Analyzed and interpreted the data; Contributed analysis tools or data; Wrote the paper.

Data availability statement

Data included in article/supp. Material/referenced in article.

Declaration of competing interest

The authors declare that they have no known competing financial interests or personal relationships that could have appeared to influence the work reported in this paper.

Acknowledgements

The authors express their gratitude to the General Directorate of Scientific Research and Technological Development (DGRSDT) for the provided support. This work is part of PRFU under the number: B00L02UN030120210003.

References

[1] Q. Lin, A. Armin, R.C.R. Nagiri, P.L. Burn, P. Meredith, Electro-optics of perovskite solar cells, Nat. Photonics 9 (2015) 106.

[2] Q. Sun, X. Gong, H. Li, S. Liu, X. Zhao, Y. Shen, M. Wang, Direct formation of I3-ions in organic cation solution for efficient perovskite solar cells, Sol. Energy Mater. Sol. Cells 185 (2018) 111–116, https://doi.org/10.1016/j.solmat.2018.05.017;
(a) M. Wang, Z. Zang, B. Yang, X. Hu, K. Sun, L. Sun, Performance improvement of perovskite solar cells through enhanced hole extraction: the role of iodide concentration gradient, Sol. Energy Mater. Sol. Cells 185 (2018) 117–123, https://doi.org/10.1016/j.solmat.2018.05.025.

[3] Lin Zhang, Yao Zhao, and Qilin Dai, Recent Progress in Perovskite Solar Cell:Fabrication, Efficiency, and Stability, https://doi.org/10.1007/978-3-030-69445-6_1)".

[4] M.A. Green, E.D. Dunlop, J.H. Ebinger, M. Yoshita, N. Kopidakis, A.H. Baillie, 'Solar cell efficiency table. (Version 55), ' Prog. Photovolt. 28 (3–15) (January 2020).

[5] S. Wang, D.B. Mitzi, C.A. Feild, A. Guloy, "Synthesis and characterization of [NH2C(I):NH2]3MI5 (M = Sn, Pb): stereochemical activity in divalent tin and lead halides containing single, in: ltbbrac.110.rtbbrac. Perovskite Sheets,", ACS Publications, 2002. May 01, https://pubs.acs.org/doi/pdf/10.1021/ja00124a012. (Accessed 25 July 2023).

[6] A. Poglitsch, D. Weber, Dynamic disorder in methyl ammonium trihalogeno plumbates (II) observed by millimeter-wave spectroscopy, J. Chem. Phys. 87 (11) (1987) 6373–6378".

[7] T. Ishihara, J. Takahashi, T. Goto, Exciton state in two-dimensional perovskite semiconductor (C10H21NH3)2PbI4, Solid State Commun. 69 (9) (1989) 933–936".

[8] N. Onoda-Yamamuro, T. Matsuo, H. Suga, Dielectric study of CH3NH3PbX3(X = Cl, Br, I), J. Phys. Chem. Solid. 53 (7) (1992) 935–939".

[9] C.R. Kagan, D.B. Mitzi, C.D. Dimitrakopoulos, Organic-inorganic hybrid materials as semiconducting channels in thin-film field-effect transistors, Science 286 (5441) (1999) 945–947".

[10] D.P. McMeekin, et al., A mixed-cation lead mixed-halide perovskite absorber for tandem solar cells, Science 351 (6269) (Jan. 2016) 151–155, https://doi.org/10.1126/science.aad5845.

[11] M. Wang, Z. Zang, B. Yang, X. Hu, K. Sun, L. Sun, Performance improvement of perovskite solar cells through enhanced hole extraction: the role of iodide concentration gradient, Sol. Energy Mater. Sol. Cell. 185 (Oct. 2018) 117–123, https://doi.org/10.1016/j.solmat.2018.05.025.

[12] U. Mandadapu, V.V. S, K. Thyagarajan, Simulation and analysis of lead based perovskite solar cell using SCAPS-1D, INDJST 10 (11) (Mar. 2017) 1–8, https://doi.org/10.17485/ijst/2017/v11i10/110721.

[13] A.S. Chouhan, N.P. Jasti, S. Avasthi, Effect of interface defect density on performance of perovskite solar cell: correlation of simulation and experiment, Mater. Lett. 221 (Jun. 2018) 150–153, https://doi.org/10.1016/j.matlet.2018.03.095.

[14] A. Babayigit, A. Ethirajan, M. Muller, B. Conings, Toxicity of organometal halide perovskite solar cells, Nat. Mater. 15 (2016) 247–251, https://doi.org/10.1038/nmat4572.

[15] Manish Kumar a,* , Abhishek Raj b.c , Arvind Kumar a , Avneesh Anshul, "An optimized lead-free formamidinium Sn-based perovskite solar cell design for high power conversion efficiency by SCAPS simulation" [Online]. Available: https://doi.org/10.1016/j.optmat.2020.110213.

[16] L.-C. Tang, C.-S. Chang, L.-C. Tang, J.Y. Huang, Electronic structure and optical properties of rhombohedral CsGeI3 crystal, J. Phys. Condens. Matter 12 (43) (Oct. 2000) 9129, https://doi.org/10.1088/0953-8984/12/43/303.

[17] M. Houari, et al., Optoelectronic properties of germanium iodide perovskites AGeI3 (A = K, Rb and Cs): first principles investigations, Opt. Quant. Electron. 51 (7) (Jun. 2019) 234, https://doi.org/10.1007/s11082-019-1949-y.

[18] I. Ornelas-Cruz, et al., DFT-based study of the bulk tin mixed-halide CsSnI3-xBrx perovskite, Comput. Mater. Sci. 178 (Jun. 2020), 109619, https://doi.org/10.1016/j.commatsci.2020.109619.

[19] Q. Zhang, H. Mushahali, H. Duan, M.-H. Lee, Q. Jing, The linear and nonlinear optical response of CsGeX3 (X=Cl, Br, and I): the finite field and first-principles investigation, Optik 179 (Feb. 2019) 89–98, https://doi.org/10.1016/j.ijleo.2018.10.159.

[20] M. Roknuzzaman, et al., Electronic and optical properties of lead-free hybrid double perovskites for photovoltaic and optoelectronic applications, Sci. Rep. 9 (1) (2019) 1–7.

[21] I. Hamideddine, N. Tahiri, O.E. Bounagui, H. Ez-Zahraouy, Ab initio study of structural and optical properties of the halide perovskite KBX3 compound, J. Korean Ceram. Soc. 59 (3) (2022) 350–358.

[22] M.M. Namisi, R.J. Musembi, W.M. Mulwa, B.O. Aduda, DFT study of cubic, tetragonal and trigonal structures of KGeCl3 perovskites for photovoltaic applications, Computational Condensed Matter 34 (Mar. 2023), e00772, https://doi.org/10.1016/j.cocom.2022.e00772.

[23] H. Bouda, T. Bahlagui, R. Masrour, L. Bahmad, A. El kenz, A. Benyoussef, Unexpected magnetic behavior of Ga doped CuFe1-xGaxO2 delafossite, x = 0.04: first principle calculation and Monte Carlo simulation, Eur. Phys. J. E 134 (10) (Oct. 2019) 543, https://doi.org/10.1140/epjp/i2019-12955-8.

[24] M. A. Abdelshakour et al., "Greenness-by-design approach for developing novel UV spectrophotometric methodologies resolving a quaternary overlapping mixture," Arch. Pharmazie, vl. n/a, no. n/a, p. e2300216, doi: 10.1002/ardp.202300216..

[25] W. Kohn, L.J. Sham, Self-consistent equations including exchange and correlation effects, Phys. Rev. 140 (4A) (1965) A1133.

[26] P.A. Penczek, F.J. Asturias, Ab initio cryo-EM structure determination as a validation problem, in: 2014 IEEE International Conference on Image Processing (ICIP), Oct. 2014, pp. 2090–2094, https://doi.org/10.1109/ICIP.2014.7025419.

[27] A.J. Cohen, P. Mori-Sánchez, W. Yang, Insights into current limitations of density functional theory, Science 321 (5890) (Aug. 2008) 792–794, https://doi.org/10.1126/science.1158722.

[28] K. Schwarz, Computation of materials properties at the atomic scale, in: Selected Topics in Applications of Quantum Mechanics, IntechOpen, 2015, https://doi.org/10.5772/59108.

[29] J.P. Perdew, K. Burke, M. Ernzerhof, Generalized gradient approximation made simple, Phys. Rev. Lett. 77 (18) (1996) 3865.

[30] G. Liu, et al., Mn 2 co z (z= al, ga, in, si, ge, sn, sb) compounds: structural, electronic, and magnetic properties, Phys. Rev. B 77 (1) (2008), 014424.

[31] R. Golesorkhtabar, P. Pavone, J. Spitaler, P. Puschnig, C. Draxl, ElaStic: a tool for calculating second-order elastic constants from first principles, Comput. Phys. Commun. 184 (8) (2013) 1861–1873.

[32] C.-Z. Fan, et al., Potential superhard osmium dinitride with fluorite and pyrite structure: first-principles calculations, Phys. Rev. B 74 (12) (2006), 125118.

[33] M.A. Fadla, B. Bentria, T. Dahame, A. Benghia, First-principles investigation on the stability and material properties of all-inorganic cesium lead iodide perovskites CsPbI3 polymorphs, Phys. B Condens. Matter 585 (May 2020), 412118, https://doi.org/10.1016/j.physb.2020.412118.

[34] F.D. Murnaghan, The compressibility of media under extreme pressures, Proc. Natl. Acad. Sci. USA 30 (9) (1944) 244–247.

[35] M. Houari, et al., Semiconductor behavior of halide perovskites AGeX 3 (A= K, Rb and Cs; X= F, Cl and Br): first-principles calculations, Indian J. Phys. 94 (2020) 455–467.

[36] R. Majumder, S. Mitro, B. Bairagi, Influence of metalloid antimony on the physical properties of palladium-based half-Heusler compared to the metallic bismuth: a first-principle study, J. Alloys Compd. 836 (2020), 155395.

[37] K.M. Hossain, S. Mitro, M.A. Hossain, J.K. Modak, M. Rasheduzzaman, M.Z. Hasan, Influence of antimony on the structural, electronic, mechanical, and anisotropic properties of cubic barium stannate, Mater. Today Commun. 26 (2021), 101868.

[38] K.M. Hossain, S. Ahmad, S. Mitro, Unraveling the effects of metal incorporation in cubic perovskite SrCoO3 by partially replacing Co atoms, Chem. Phys. Lett. 786 (2022), 139208.

[39] G. Yang, J. Yang, Y. Yan, Y. Wang, The relationship between the electronic structure and thermoelectric properties of Zintl compounds M 2 Zn 5 as 4 (M= K, Rb), Phys. Chem. Chem. Phys. 16 (12) (2014) 5661–5666.

[40] G. Xing, J. Sun, Y. Li, X. Fan, W. Zheng, D.J. Singh, Electronic fitness function for screening semiconductors as thermoelectric materials, Phys. Rev. Mater. 1 (6) (Nov. 2017), 065405, https://doi.org/10.1103/PhysRevMaterials.1.065405.

[41] G. Xing, J. Sun, Y. Li, X. Fan, W. Zheng, D.J. Singh, "Erratum: electronic fitness function for screening semiconductors as thermoelectric materials [Phys. Rev. Materials 1, Phys. Rev. Mater. 1 (7) (2017), 065405, https://doi.org/10.1103/PhysRevMaterials.1.079901, 079901, Dec. 2017.

[42] Y. Li, L. Zhang, D.J. Singh, New stable ternary alkaline-earth metal Pb(II) oxides: Ca/Sr/BaPb2O3 and BaPbO2, Phys. Rev. Mater. 1 (5) (Oct. 2017), 055001, https://doi.org/10.1103/PhysRevMaterials.1.055001.

[43] U.-G. Jong, C.-J. Yu, Y.-H. Kye, Y.-G. Choe, W. Hao, S. Li, First-principles study on structural, electronic, and optical properties of inorganic Ge-based halide perovskites, Inorg. Chem. 58 (7) (Apr. 2019) 4134–4140, https://doi.org/10.1021/acs.inorgchem.8b03095.
[44] J. Wang, S. Yip, S.R. Phillpot, D. Wolf, Crystal instabilities at finite strain, Phys. Rev. Lett. 71 (25) (1993) 4182.
[45] R. Hill, The elastic behaviour of a crystalline aggregate, Proc. Phys. Soc. 65 (5) (1952) 349.
[46] J. Hafner, Materials simulations using VASP—a quantum perspective to materials science, Comput. Phys. Commun. 177 (1–2) (2007) 6–13.
[47] D. Pettifor, Theoretical predictions of structure and related properties of intermetallics, Mater. Sci. Technol. 8 (4) (1992) 345–349.
[48] A. Abada, K. Amara, S. Hiadsi, B. Amrani, First principles study of a new half-metallic ferrimagnets Mn2-based full Heusler compounds: Mn2ZrSi and Mn2ZrGe, J. Magn. Magn Mater. 388 (Aug. 2015) 59–67, https://doi.org/10.1016/j.jmmm.2015.04.023.
[49] M. Afsari, A. Boochani, M. Hantezadeh, Electronic, optical and elastic properties of cubic perovskite CsPbI3: using first principles study, Optik 127 (23) (Dec. 2016) 11433–11443, https://doi.org/10.1016/j.ijleo.2016.09.013.
[50] S.I. Ranganathan, M. Ostoja-Starzewski, Universal elastic anisotropy index, Phys. Rev. Lett. 101 (5) (2008), 055504.
[51] A. Anjami, A. Boochani, S.M. Elahi, H. Akbari, Ab-initio study of mechanical, half-metallic and optical properties of Mn2ZrX (X=Ge, Si) compounds, Results Phys. 7 (Jan. 2017) 3522–3529, https://doi.org/10.1016/j.rinp.2017.09.008.
[52] A. Hamidani, B. Bennecer, B. Boutarfa, Structural and elastic properties of the half-Heusler compounds IrMnZ (Z=Al, Sn and Sb), Mater. Chem. Phys. 114 (2) (Apr. 2009) 732–735, https://doi.org/10.1016/j.matchemphys.2008.10.038.
[53] K. Benkaddour, et al., First-principles study of structural, elastic, thermodynamic, electronic and magnetic properties for the quaternary Heusler alloys CoRuFeZ (Z = Si, Ge, Sn), J. Alloys Compd. 687 (Dec. 2016) 211–220, https://doi.org/10.1016/j.jallcom.2016.06.104.
[54] N. Ravindra, P. Ganapathy, J. Choi, Energy gap–refractive index relations in semiconductors–An overview, Infrared Phys. Technol. 50 (1) (2007) 21–29.
[55] S. Ozaki, S. Adachi, Optical constants of ZnS x Se1− x ternary alloys, J. Appl. Phys. 75 (11) (1994) 7470–7475.
[56] S. Saib, N. Bouarissa, P. Rodríguez-Hernández, A. Muñoz, Structural and dielectric properties of AlN under pressure, Phys. B Condens. Matter 403 (21–22) (2008) 4059–4062.
[57] A. Gueddim, S. Zerroug, N. Bouarissa, Optical characteristics of ZnTe1− xOx alloys from first-principles calculations, J. Lumin. 135 (2013) 243–247.
[58] Q. Mahmood, N.A. Noor, M. Rashid, B.U. Haq, A. Laref, I. Qasim, Physical properties of alkali metals-based iodides via Ab-initio calculations, J. Phys. Chem. Solid. 132 (Sep. 2019) 68–75, https://doi.org/10.1016/j.jpcs.2019.04.005.
[59] S.A. Khandy, D.C. Gupta, Structural, elastic and thermo-electronic properties of paramagnetic perovskite PbTaO 3, RSC Adv. 6 (53) (2016) 48009–48015.
[60] B.U. Haq, R. Ahmed, S. AlFaify, F.K. Butt, A. Shaari, A. Laref, Exploring thermoelectric materials for renewable energy applications: the case of highly mismatched alloys based on AlBi1-xSbx and InBi1-xSbx, Intermetallics 93 (2018) 235–243.